Ultrasonics 93 (2019) 26–36

Contents lists available at ScienceDirect

Ultrasonics

journal homepage: www.elsevier.com/locate/ultras

A real-time data-based scan conversion method for single element ultrasound transducers

Gergely Csány[a,*], Klára Szalai[b], Miklós Gyöngy[a]

[a] Faculty of Information Technology and Bionics, Pázmány Péter Catholic University, Budapest, Hungary
[b] Department of Dermatology, Venerology and Dermatooncology, Semmelweis University, Budapest, Hungary

ARTICLE INFO

Keywords:
Single-element transducer
Image formation
Freehand scanning
Scan conversion
Correlation

ABSTRACT

The current work investigates the performance of a real-time scan conversion algorithm for generating a 2-D ultrasound image from a laterally scanned single-element ultrasound transducer, which has applications in point-of-care devices such as for skin imaging. The algorithm employs a fixed calibration curve to update a predefined image grid in real time. Simulations showed that the calibration curve (with a maximum of 1) is robust to changes in scatterer concentration (8.3×10^{-3} mean absolute error), signal to noise ratio (1.0×10^{-3} mean absolute error for -5 dB SNR), and can be accurately predicted from a small number (31) of point scatterers (6.9×10^{-3} mean absolute error). Good agreement was also found between the calibration curves obtained from simulated and experimental data (1.19×10^{-2} mean absolute error). The scan conversion algorithm was validated by evaluation of the position estimation errors on both simulations and experiments. Clinical images of skin lesions (N = 20) demonstrate the feasibility of the algorithm for real, non-homogeneous tissue. Use of a fixed calibration curve compared to an adaptive calibration curve gave similar accuracies in the scanning step size range of 150–350 μm (with an average overlap of the accuracy ranges of 92.94% for simulations and 42.83% for experiments), and a 350-fold improvement in computation time.

1. Introduction

In ultrasound as in other medical diagnostics, there is a trend towards making portable and cost-effective devices that offer better access to healthcare [1–3]. One method of reducing cost is to substitute electronic scanning of the A-lines for physical scanning, either using mechanical scanning with a stepper motor [4] or freehand scanning [5]. Typically, only one transducer element is required for physical scanning, which is especially advantageous for higher frequencies (>20 MHz), where transducer array manufacture is still relatively complex [6]. Since single-element transducers have poor lateral resolution outside their focal region, an annular array may also be used; this achieves a more uniform lateral focussing with depth while requiring lower transducer and hardware complexity than widely used linear arrays [7].

Regarding mechanical scanning, the presence of the motor and driving circuity increase cost, complexity, and power consumption while reducing reliability [8]. Alternatively, freehand scanning may be used, where estimates of the scan position are necessary. One option is to use some type of location or motion sensor, which could be acoustic [9], magnetic [10,11], electromagnetic [12,13], tilt [14,8,15–17], optical, or infrared [18]. However, these sensors usually suffer from some combination of issues including limited position accuracy, latencies in either position sensing or ultrasound data recording, or limitations on the scanning path that can be covered [19]. In one commercially successful application, the Signos system [8] relies on an angularly scanned transducer with a tilt sensor. However, for applications involving areas of interest relatively close to the transducer and containing angle-dependent surface reflectors, linear scanning may be more appropriate. One such application is the examination of skin surface lesions [20].

Another potential method of estimating position during freehand scanning involves use of the data to estimate position [9], which we term data-based scanning, or DABAS. In current practice, a calibration curve describing the degree of similarity between two 2-D ultrasound images as a function of their distance allows an estimate of their relative positions. Such estimates from a set of 2-D images are combined to generate a scan-converted 3-D volume. Our group is generalizing this idea to the scan conversion of a set of A-lines into a 2-D image. In such a situation, it becomes a user need to visualize the image in real-time. Therefore, we have developed a real-time DABAS algorithm [21] that accepts A-lines into a predefined image grid as soon as they arrive rather than the classical method of performing offline processing on all the data. In a previous article by our group, we presented a clinical

* Corresponding author.
E-mail addresses: csany.gergely@itk.ppke.hu (G. Csány), gyongy.miklos@itk.ppke.hu (M. Gyöngy).

https://doi.org/10.1016/j.ultras.2018.10.006
Received 17 May 2018; Received in revised form 11 October 2018; Accepted 15 October 2018
Available online 16 October 2018
0041-624X/

prototype for imaging skin using this algorithm [22]. The aim of the current article is to validate this real-time algorithm on simulations and experiments.

The remainder of the article is structured as follows. The next section begins with an overview of classical DABAS methods. This is followed by a presentation of our real-time DABAS method, including the derivation of the calibration curve, the scan conversion method, and measures of position estimation errors. In the subsequent Materials and Methods section, the data acquisition during the simulations as well as phantom and *in vivo* skin experiments is detailed. The data are used to investigate two questions: the accuracy of the calibration curve estimate and the performance of the real-time DABAS algorithm. Furthermore, the performance is tested using a fixed calibration curve as well as an adaptive calibration curve (as taken from [23]) to see whether the fixed calibration curve can provide a comparable accuracy while ensuring real-time operation. We note that although our current motivating application is skin imaging, there exist other potential applications such as non-destructive testing. Moreover, the method may also be applied on annular array transducers.

2. Real-time data-based scan conversion (DABAS)

2.1. Overview of existing DABAS methods

As previously mentioned, a method of estimating transducer motion during freehand scanning relies on quantifying the change of the incoming ultrasound data as it is moved and relating this change to transducer displacement using a calibration curve. For generality between the classical problem of converting 2-D images into a 3-D image and our problem of converting 1-D A-lines into a 2-D image, the term data frame will be used to refer to individual A-lines or 2-D images, sets of which need to be aligned in space to perform scan conversion. Before considering the theory and implementation of the current method, existing methods of calibration curve estimation and transducer position estimation for scan conversion are briefly considered.

The calibration curve $\rho(d)$ is a function expressing the level of similarity ρ between two data frames whose recording location is a distance d apart. The measure of similarity is usually the Pearson correlation coefficient, so that if fully developed speckle can be assumed, then the calibration curve is the lateral autocorrelation of the imaging system point spread function. If the fully developed speckle assumption does not hold, more advanced estimation methods may need to be employed, including statistical modeling of speckle formation [24,25], tissue characterization [26], adaptive models [27,23], or machine learning [28]. It is unclear, however, how general these methods are to different tissues or transducer types, or indeed how large errors are incurred when assuming fully developed speckle for single element transducers. It would be desirable, therefore, to investigate the potential limitations of assuming fully developed speckle for single element transducers.

Another issue to consider is the method of scan conversion. Due to the presence of noise, an estimate of the distance between two subsequent data frames based on the estimated calibration curve $\tilde{\rho}^{-}(d)$ is sometimes considered too erroneous. Therefore, current methods combine distance estimates between many pairs of data frames using weighted averages [29–32]. Again, it is unclear how accurate position estimation is for noisy data from single element transducers, whereas the retrospective combination of distance estimates compromises real-time scan conversion. Therefore, a novel, real-time DABAS algorithm [21] is proposed that displays a data frame in the relevant place as soon as it is recorded.

2.2. Calibration curve

Let the calibration curve $\rho(d)$ be defined as the expected correlation coefficient between a reference data frame and a data frame recorded at a distance d from the reference. When fully developed speckle is assumed without the presence of imaging noise, $\rho(d)$ is independent of the reference recording location and its extrema are:

$$\rho(0) = 1, \tag{1}$$

$$\lim_{d\to\infty} \rho(d) = 0, \tag{2}$$

where $\rho(0)$ concerns the correlation coefficient between two data frames recorded at different times but at the same location. This distinction becomes important when additive noise is present, whereupon the first extremum is modified as follows:

$$\rho(0) = \sqrt{\frac{10^{\sigma/20}}{1 + 10^{\sigma/20}}}, \tag{3}$$

where σ is the signal-to-noise ratio (SNR) in dB.

With the addition of noise, the estimation of the calibration curve will be subject to sampling error. Moreover, due to statistical fluctuations, the correlation coefficient ρ between two data frames at distance d will differ from $\rho(d)$ even without the presence of noise. Lastly, when fully developed speckle cannot be assumed (conventionally defined as less than 10 scatterers per resolution cell [33]), the autocorrelation of the scattering function will modify $\rho(d)$. The extent of all these phenomena should be assessed using simulations. In addition, two hypotheses concerning $\rho(d)$ should be tested. First, $\rho(d)$ should be closely related to the lateral autocorrelation of the imaging response to a combination of points at several depths. Second, when the calibration curve under noise is normalized to a maximum of 1, the curve should return to its original shape that it had without the addition of noise.

2.3. Real-time DABAS algorithm

Once an estimate of the calibration curve $\rho(d)$ has been obtained, a scan conversion algorithm may be employed on the incoming data frames $F_1, F_2, \ldots, F_I$. In conventional DABAS methods [29–32], the correlation coefficients between all or a subset of the data frames are first calculated; these coefficients are then combined offline to measure the relative positions between subsequent data frames; lastly, the data frames are interpolated onto image frames $I_1, I_2, \ldots, I_K$ with a regular spacing of Δy between them. In contrast, the current algorithm, described in detail in [21], relies on a high enough frame rate of data frame acquisition to yield the assumption that for each image column, there will be a data frame recorded sufficiently close to the desired location. The real-time algorithm employs an acceptance criterion $\alpha_{i,k}$ that determines whether the current data frame i can be loaded into the current image column k:

$$\alpha_{i,k} = \sum_{j=1}^{J} w\left(j, J\right) \left| \rho_{I_{k-j}, F_i} - \rho\left(j\Delta y\right) \right| < \epsilon, \tag{4}$$

where $w(j)$ are a set of weights for a window size J, used for combining the absolute differences between a measured correlation coefficient ρ_{I_{k-j},F_i} and an expected correlation coefficient $\rho(j\Delta y)$. The measured correlation coefficient ρ_{I_{k-j},F_i} is calculated between the current data frame F_i and J past image frames. If the data frame was recorded at the expected location, then the expected correlation coefficient should be$\rho(j\Delta y)$. When the weighted sum of absolute differences is below some predefined threshold ϵ, the acceptance criterion is met, the current data frame is loaded into image frame I_k, and k is incremented by 1 in order to search for the data frame that can load the next image frame.

The above, relatively simple algorithm raises several questions. What estimation errors does the algorithm produce? Is there an optimum image column spacing Δy that minimizes position estimation errors? In order to make the investigation of these questions manageable, the current work restricts itself to a window size of $J = 1$. A discussion of error quantification follows.

2.4. Position estimation errors

When loading the data frames recorded at true positions $\mathbf{x}_t$ into image columns at desired positions $\mathbf{x}_d$, the difference between the two vectors gives rise to position estimation errors and thus image degradation. A simple scalar measure of error is the root mean square error $\|\mathbf{x}_t - \mathbf{x}_d\|_2$. However, the error encapsulates two different phenomena that should be differentiated from each other. The first, which we term *bias error*, describes the linear increase in error between the true and desired positions as a function of the desired position. This bias error can be quantified by fitting a line to the relationship between $\mathbf{x}_t$ and $\mathbf{x}_d$ and is measured in %:

$$e_b = \underset{e}{\operatorname{argmin}} \|\mathbf{x}_t - e\mathbf{x}_d\|_2. \tag{5}$$

After removing the overall bias from the estimation, the average position error will be zero. However, from one image column to the next, the A-line may still be selected too early or too late. We term this fluctuating error the *ripple error* and define it as the root mean square position error after correcting for bias:

$$e_r = \|\mathbf{x}_t - e_b\mathbf{x}_d\|_2. \tag{6}$$

By measuring the bias and ripple errors of the algorithm, the feasibility of using this real-time DABAS algorithm for single element transducer imaging may be investigated using simulations and experiments.

2.5. Translation speed requirements

One aspect of the algorithm that has not yet received attention is the issue of how fast the transducer can be translated for the algorithm to still function properly. For an image grid step size (Δy), the pulse repetition frequency (*PRF*) of the ultrasound imaging system should be fast enough that several (n) frames be recorded over a distance Δy to provide adequate sampling:

$$v \leqslant \Delta y / n \cdot PRF. \tag{7}$$

As will be seen later, the choice of Δy will itself depend on the calibration curve.

3. Materials and methods

3.1. Ultrasound data recordings

In order to investigate the variability of the calibration curve and accuracy of position estimation during scan conversion, both simulations and phantom experiments were performed. In both cases, a series of A-lines were collected by laterally moving the transducer in 10 μm steps. In addition, clinical experiments were performed to investigate the accuracy of the scan conversion method in real tissue.

3.1.1. Simulations

Simulations were performed using the Field II software [34,35] with the same transducer geometry and response as used in the experiments. To find the transducer response, backscatter from a planar plexiglass element placed at the focus of the real transducer was recorded. A 4–12 MHz brick-wall filter was applied by transforming the signals into the frequency domain and setting coefficients outside the 4–12 MHz frequency band to zero. Then, an f^3 correction was applied to account for the planar shape of the plexiglass reflector [36,37]. Prior to analysis, both experimental and simulated radiofrequency (RF) data were again filtered using the same 4–12 MHz brick-wall filter.

3.1.2. Phantom experiment

The experimental setup consisted of a single element transducer (V317, Olympus, Tokyo, Japan; diameter: 6.3 mm; f#: 3) connected to a pulser-receiver-digitizer (US-KEY, LeCoeur, Chuelles, France) with pulse width setting 5 and transmit voltage 120 V. The pulser-receiver-digitizer was connected to a laptop that stored the received RF data at 80 MHz sampling rate using custom-written software.

It should be mentioned that the central frequency of the Olympus V317 transducer is 20 MHz; however, due to the lower frequency response of the US-KEY device, the overall response of the system in the 4–12 MHz range was around 11 times larger than around 20 MHz. Therefore, to have a signal centered around one frequency and with an acceptable SNR, the filter described in Section 3.1.1 was used – both for simulations and experiments. Since our main conclusions here are independent of the frequencies used, the demonstrated method can be similarly applied for high frequency imaging which is one of the motivations of our work (Section 1).

Transducer motion was achieved using a precision mechanical motion system (MTS50/M-Z8, Thorlabs, Newton, NJ). Measurements were carried out in a deionized water bath for acoustic coupling.

For the phantom experiment, a homogeneous agar-graphite phantom was prepared. Deionized water was heated to above 80 °C in a microwave, slowly adding 3% w/w agar, and then 4% w/w graphite to the water while gently stirring, then pouring the mixture into a plexiglass cast and allowing to cool. Upon cooling and removal from the cast, a 25 mm (axial) × 66 mm (lateral) × 45 mm (elevational) phantom was obtained.

3.1.3. Preliminary in vivo human skin experiment

In vivo human skin experiments were performed at the Department of Dermatology, Venereology and Dermatooncology, Semmelweis University. The transducer and pulser-receiver digitizer described in the previous subsection was placed inside a plastic housing and manually scanned over the surface of the skin [22]. The received A-lines were then recorded on a laptop. B-mode images of the same skin lesion were also recorded using a reference commercial ultrasound imager (EUP-L75 connected to Hitachi Preirus, Hitachi, Tokyo, Japan). To ensure accurate comparison, the maximal lateral extent of the lesion was sought to be imaged using both systems. The experiments were carried out as part of an ethically approved study. The current work presents the analysis of N = 20 lesions.

Prior to lateral scan conversion (based on data-based position estimation), the same 4–12 MHz brick-wall filter was applied on clinical data as in simulations and phantom experiments. To compensate for undesired axial motion during manual scanning, the cross-correlation peak between adjacent lines was used to axially shift each incoming A-line.

3.2. Calibration curve

A number of real and simulated ultrasound images were generated, from which calibration curves were obtained in the following manner. First, for each (depth) index, the cross-correlation of each RF line (acting as reference) was calculated in the lateral direction using adjacent RF lines within a lateral range of 600 μm. The mean of these cross-correlation curves was then calculated across all depths and across all reference RF lines.

Calibration curves were simulated to seek answers to the following questions (described in the subsections below).

3.2.1. Scatterer density

To answer the question of how the violation of the fully developed speckle (FDS) assumption affects the calibration curve (Section 2.2), a number of homogeneous phantoms were simulated with different scatterer densities. The scatterer densities were calculated in terms of the resolution cell [38].

3.2.2. Signal to noise ratio

In order to investigate the noise-dependence of the calibration curve estimate – and by extension, the robustness of the real-time DABAS algorithm to additive noise – the same Gaussian random noise was

added to the RF image data producing various signal-to-noise ratios. To answer the question of whether the addition of noise preserves the shape of the calibration curve (Section 2.2), the curve was normalized to have a maximum value of 1 and compared with the noiseless calibration curve.

3.2.3. Calibration curve estimation from point scatterers

If the imager response were depth-invariant, then we would expect from the Van Cittert-Zernike theorem that the calibration curve obtained from a single scatterer would correspond to that obtained from fully developed speckle [39]. However, due to depth-dependence, it is postulated that the placement of several scatterers at depths far enough to avoid interference will approximate the calibration curve of the fully developed speckle case (Section 2.2). Therefore, we simulated images from a number of scatterers and compared how closely the corresponding calibration curve could approximate the true calibration curve.

3.2.4. Comparison of simulation with experiment

To test how well simulations reflect experiments, including the ability to predict the experimental calibration curve, the calibration curve from the simulated fully developed speckle image was compared with the calibration curve obtained from the experimental homogeneous phantom.

3.3. Scan conversion algorithm and its performance

3.3.1. Algorithm implementation

The real-time DABAS algorithm described in Section 2.3 was applied to the simulated and experimental homogeneous phantoms using a comparison window length $J = 1$ and a range of image grid spacings $\Delta y = 10, 20, \ldots, 600\ \mu$m. Each grid spacing corresponded to a value of cross-correlation (from the calibration curve) that was used to decide whether the current RF line should be loaded into the image grid. The bias and ripple errors were calculated for each Δy to search for an optimum Δy. The error levels were compared between simulations and experiment.

3.3.2. Comparison with adaptive calibration curve calculation

The accuracy of position estimation with a fixed calibration curve was compared with that of an adaptive calibration curve estimation method from literature [23]. The adaptive algorithm relaxes the FDS assumption by assuming that scatterer coherency is isotropic so that the local lateral coherency can be estimated from the axial autocorrelation, allowing adaptive modification of the calibration curve. The method had been developed and tested for 2-D to 3-D scan conversion and was adapted to the current case of 1-D to 2-D scan conversion in the following manner.

For each incoming A-line, comparison of the current axial autocorrelation with a reference mean axial autocorrelation of the FDS simulation phantom (10 scatterers/resolution cell) yields an estimate of the local scatterer coherency. This estimate is then used to adapt the estimated calibration curve according to the procedure described in [23]. For estimating coherency, axial autocorrelation was calculated for the envelope of data frames. Correlation of coherence was considered four times wider laterally than axially since the resolution cell was approximately four times wider in the lateral direction than in the axial.

It should be noted that apart from the use of an adaptive calibration curve, all other aspects of the implementation followed the proposed real-time DABAS algorithm, rather than the description in [23]. In particular, no angular correction was employed by using several image patches; no median filter was applied; and data frames were accepted into the image columns according to Eq. (4).

When performing comparison of the two methods, we focused on a range of step sizes where errors were minimal for both algorithms, due to maximal slope of the calibration curve [40,41]. Our aim was to investigate whether the fixed calibration curve could yield comparable accuracies while ensuring a real-time operation.

3.3.3. Evaluation of clinical data

Following collection and preprocessing of clinical data (described in Section 3.1.3), lateral scan conversion was performed on the preprocessed set of A-lines. An image grid step size of 300 μm was used, corresponding to a correlation value of 0.5 in the calibration curve. The value was evaluated from the calibration curve of the homogeneous phantom experiment, since it was assumed that the same noise level needed to be corrected for in both cases (Section 3.2.4).

For clinical data of real tissue acquired via freehand manual scanning, the exact positions of A-lines were not known *a priori*, and position errors could therefore not be estimated directly. However, using images made of the same skin lesion by the reference device, spatial dimensions of the lesions (measured manually on the images) could be used as a basis of comparison. It was expected that lesion length errors (calculated in the lateral dimension) would primarily express the inaccuracy of scan conversion, while lesion thickness errors (calculated in the axial direction) could serve as a measure of baseline error (such as arising from inaccuracies in imaging the same maximal diameter 2-D slice of the lesion volume, or the inaccuracy of manual measurements).

4. Results and discussion

Following the structure of Section 3, results are presented in terms of the ultrasound images, the calibration curves, and scan conversion algorithm performance results obtained.

4.1. Ultrasound image recordings

Fig. 1 shows simulated images of homogeneous phantoms with different scatterer densities of 0.2, 1, 5 and 10 scatterers/resolution cell, with the last case (10 scatterers/resolution cell) considered as fully developed speckle [33]). The depth of field can be qualitatively observed as a vertical band of relatively higher intensity speckle. The asymptotic behaviour towards fully developed speckle can also be qualitatively observed.

Simulated B-mode images of 1, 11 and 31 scatterers can be observed in Fig. 2. These were used to generate calibration curves that

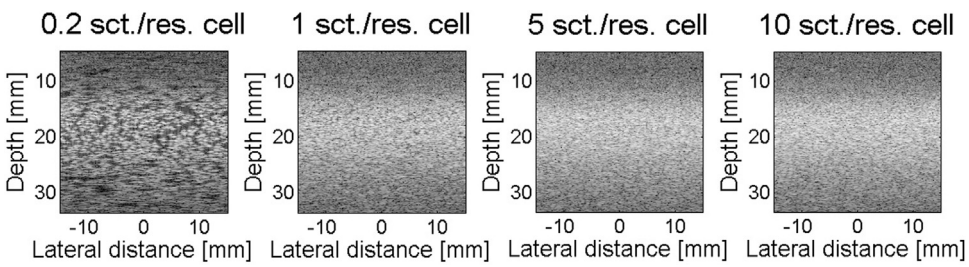

Fig. 1. Simulated B-mode images (with 60 dB dynamic range) of homogeneous phantoms of 0.2, 1, 5 and 10 scatterers/resolution cell densities, respectively. The simulated imaging system was a single element Olympus V317 transducer moved along the lateral dimension, collecting A-lines with an equal 10 μm spacing.

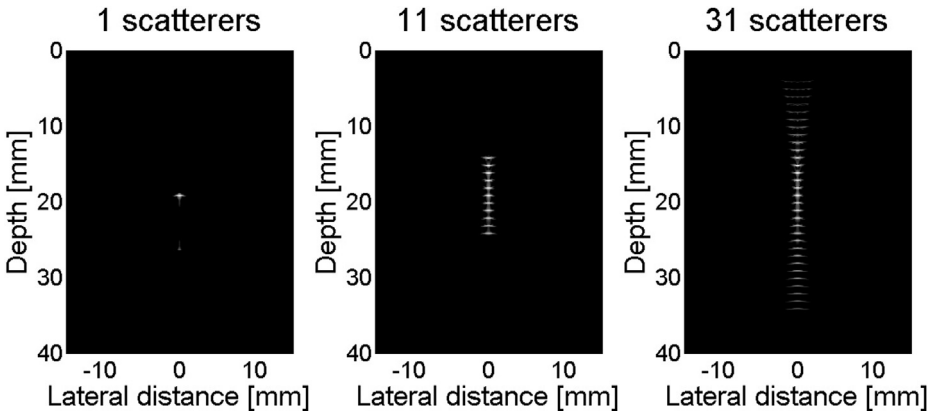

Fig. 2. Simulated B-mode images (40 dB dynamic range) of 1, 11 and 31 scatterers respectively placed around transducer focus with a uniform axial spacing of 1 mm. The imaging system simulated was the same as for Fig. 1.

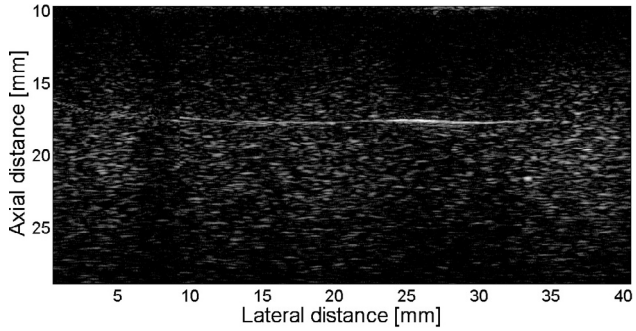

Fig. 3. B-mode ultrasound image made of a 3% agar – 4% graphite homogeneous phantom by mechanically scanning an Olympus V317 single element transducer (with 19 mm focus). The image consists of 4000 A-lines with 10 μm spacing. The depth range shown here is the range used for later analysis (calculation of the calibration curve and position estimation).

potentially approximate the fully developed scatterer case. The case of 11 scatterers approximately covers the −6 dB depth of field of the transducer. In Fig. 3, an image of the experimental agar-graphite phantom can be observed.

4.2. Calibration curve

4.2.1. Scatterer density

Calibration curves were calculated for a number of homogeneous phantoms simulated with different scatterer densities.

In order to define scatterer densities in terms of a number of scatterers in the resolution cell, the latter was established by simulating a point scatterer at the focus of the transducer, taking the envelope of the image thus produced, and calculating the area above or equal to 0.5 (or −6 dB) of the peak amplitude. Using this measure, the appropriate number of point scatterers was randomly placed on a 30 mm (axial) × 35 mm (lateral) 2-D region using a 2-D uniform distribution. Phantoms with different scatterer densities of 0.2, 1, 5 and 10 scatterers/resolution cell were generated, with the last case considered as fully developed speckle [33]. The running time of the simulations on a laptop (Intel Core i5 processor, 8 GB RAM) was 10–450 min, depending on scatterer density.

Calibration curves calculated for different scatterer densities (0.2, 1, 5, 10 scatterers/ resolution cell) were found to be almost identical (Fig. 4), with a mean absolute error of 8.3×10^{-3} (in average, for all pairs of the four curves presented). The results suggest that the real-time DABAS algorithm can use the fully developed speckle (FDS) calibration curve for a wide variety of homogeneous scatterer densities.

4.2.2. Signal to noise ratio

Calibration curves calculated from the same image with different levels of additive noise (20, 15, 10, 5, 0 and −5 dB) are presented in the top of Fig. 5. The results are shown for 10 scatterers/resolution cell but are representative for other scatterer concentrations as well. The peak correlation values are in agreement with the values expected from Eq. (3). Upon normalization to a peak value of 1 (bottom of Fig. 5), the correlation curve follows the shape of the noiseless case (with 1.0×10^{-3} mean absolute error between the noiseless-case curve and the normalized curve calculated for the −5 dB SNR case). This suggests that only a minor modification of the noiseless-case calibration curve is needed when running the DABAS algorithm in the presence of noise.

4.2.3. Calibration curve estimation from point scatterers

As introduced in Section 3.2.3, calibration curve approximation from the imaging response for a combination of point scatterers was investigated.

Since the observed amplitude in the image will decrease as the depth of the scatterer moves away from the focus, the question arises as to what depth range the scatterers need to cover to approximate the fully developed speckle calibration curve. To this end, 1, 3, …, 31 scatterers were placed in an axial line around the transducer focus, with 1 mm spacing between them (to avoid interference).

In Fig. 6, calibration curves calculated from images of 1, 11 and 31 scatterers (placed as described above and shown in Fig. 2) are presented and compared to the one calculated from a (30 mm deep) homogeneous phantom with 10 scatterers/resolution cell concentration, considered to exhibit fully developed speckle (FDS). As the number of scatterers – and thereby axial range – increases, the calibration curve approaches the FDS calibration curve, with 6.9×10^{-3} mean absolute error between the curves calculated for the 31 scatterers and for the FDS phantom. The results show that the FDS calibration curve can be approximated accurately by placing a relatively small number of scatterers along the transducer axis.

In related work (where 2-D images are extended to 3-D images), the images of simulated or real phantoms are divided into patches, and the curves are calculated separately for each patch [23,24,42]. The patch dimensions are chosen such that there is minimal variation of the calibration curve within the patch. In contrast, the current work shows how an overall FDS calibration curve may be derived for the entire region from a relatively few number of scatterers.

4.2.4. Comparison of simulation with experiment

The calibration curve calculated from experimental data is presented in the top of Fig. 7. From Eq. (3), the SNR is estimated as 10.5 dB. The bottom of Fig. 7 shows a comparison of the normalized experimental calibration curve with the FDS calibration curve from

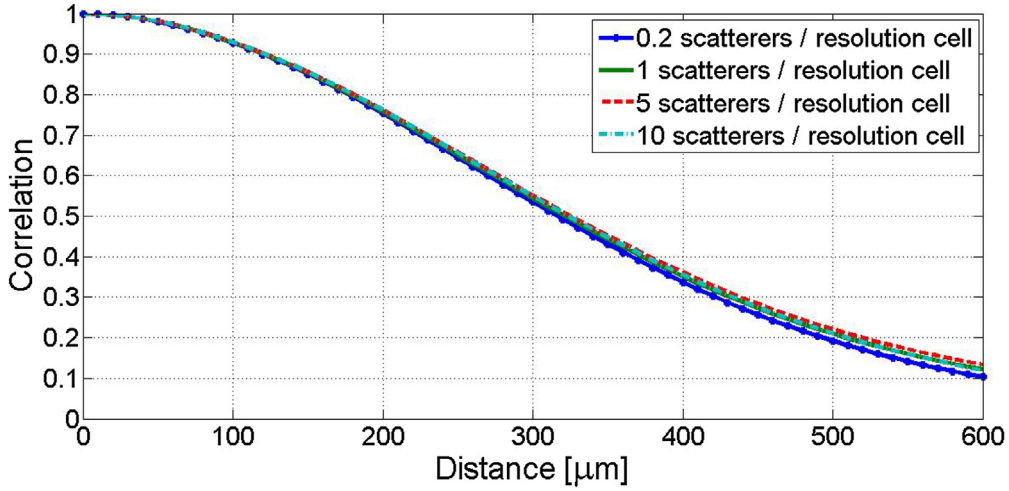

Fig. 4. Calibration curves calculated from simulated data of homogeneous phantoms with 0.2, 1, 5 and 10 scatterers/ resolution cell densities.

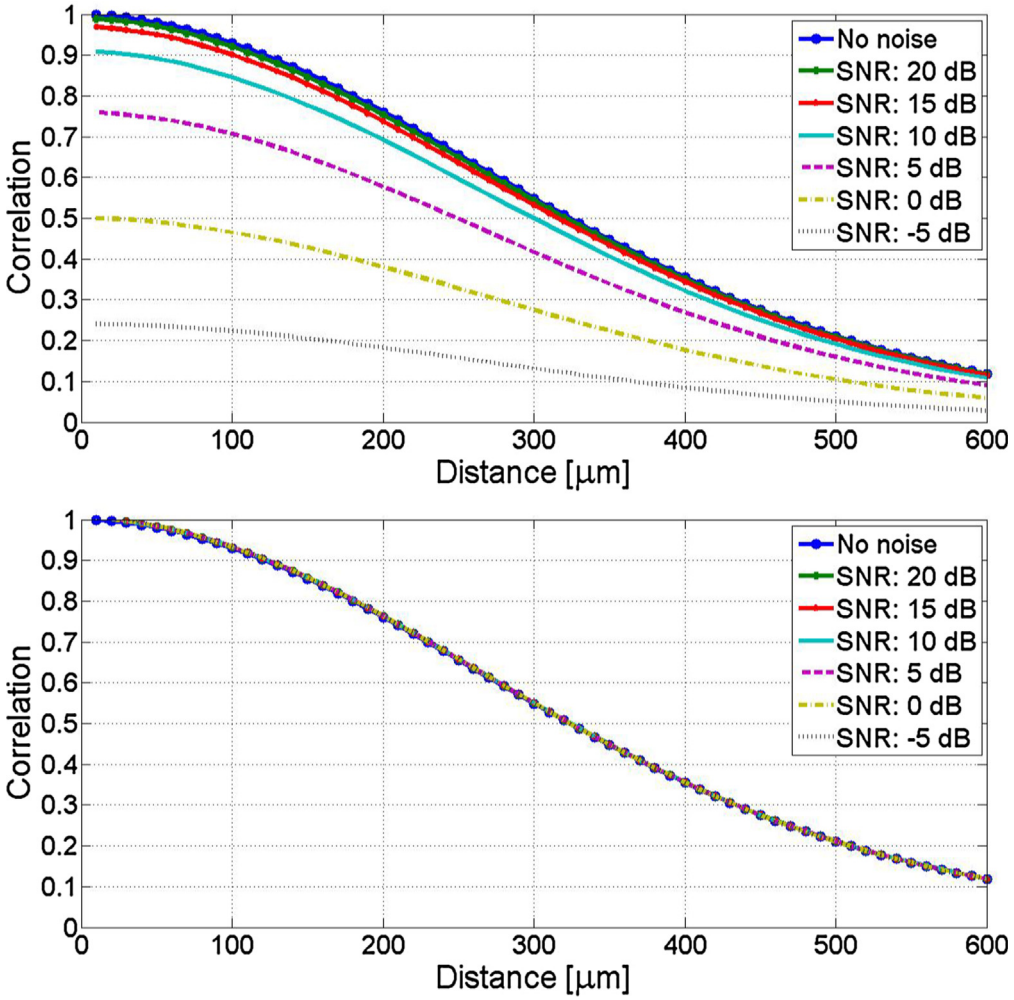

Fig. 5. Calibration curves calculated from simulated image data of homogeneous phantom (with 10 scatterers/ resolution cell density) without noise and with additional (Gaussian random distribution) noise according to 20 dB, 15 dB, 10 dB, 5 dB, 0 dB and –5 dB SNR. **Top:** Calibration curves are presented as calculated (containing also noise level information in initial decay). **Bottom:** Normalized calibration curves in order to make a visual comparison of the decay rate similarity for the curves.

simulations. The two curves show strong similarity, with 1.19×10^{-2} mean absolute error, suggesting the potential of accurate calibration curve estimation from knowledge of the transducer geometry and response.

4.3. Scan conversion algorithm performance

For the scan conversion on the simulated and phantom data, the calibration curve obtained from the FDS simulation was used; however,

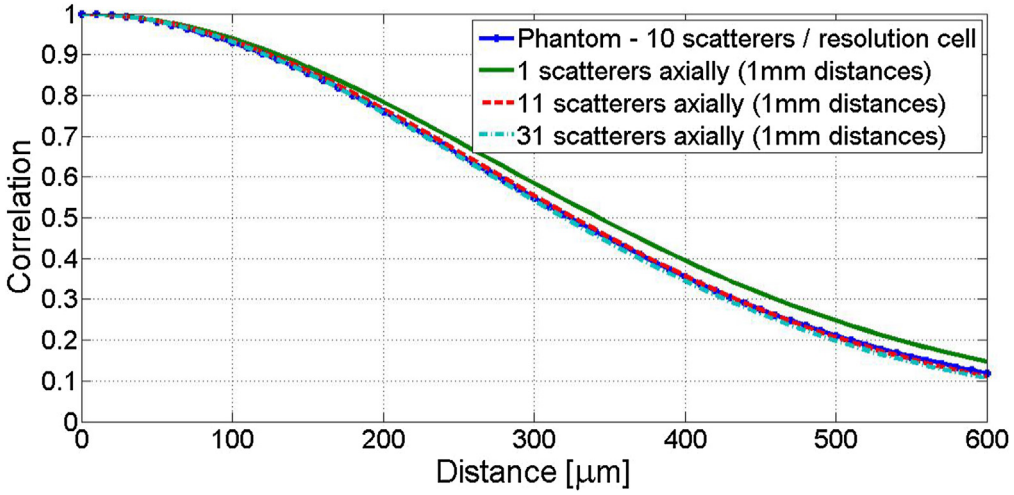

Fig. 6. Calibration curves calculated from simulated image data of 1, 11 and 31 scatterers placed axially around transducer focus with a uniform 1 mm distance are compared with calibration curve calculated from simulated image of a FDS homogeneous phantom (10 scatterers/ resolution cell density) as a reference.

in the latter case, the curve was scaled according to Eq. (3) to account for the noise level being present.

Fig. 8 shows the position estimation errors from using a fixed calibration curve in comparison to the adaptive calibration curve, on the homogeneous phantom with 10 scatterers/resolution cell. The results are representative of other scatterer densities. Using image grid step sizes that correspond to correlation values close to 1 or 0 cause relatively large errors. This result is consistent with previous work [40,41]

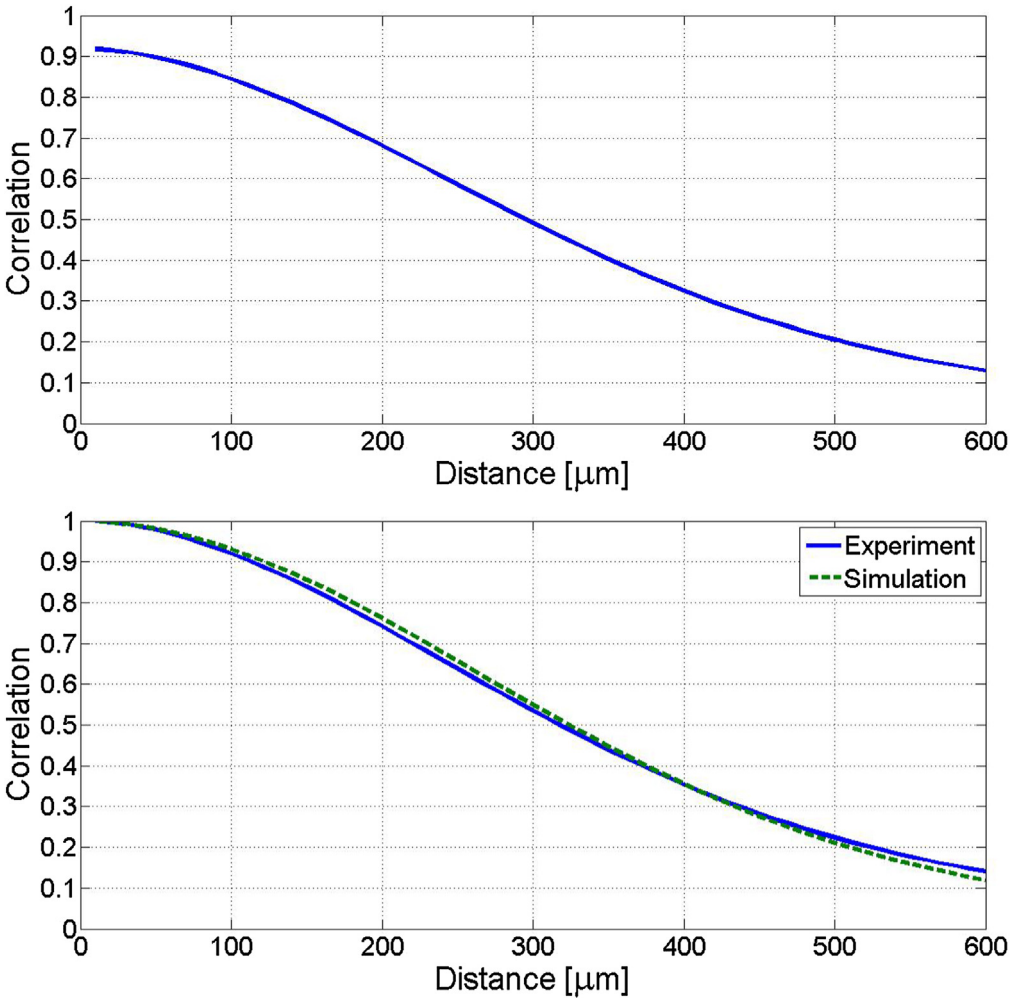

Fig. 7. Calibration curve from experimental image data. *Top:* Calibration curve calculated from experimental image data (containing noise level information in its initial decay). *Bottom:* Normalized calibration curve from experimental data compared to calibration curve from simulated data (homogeneous phantom with 10 scatterers/resolution cell density).

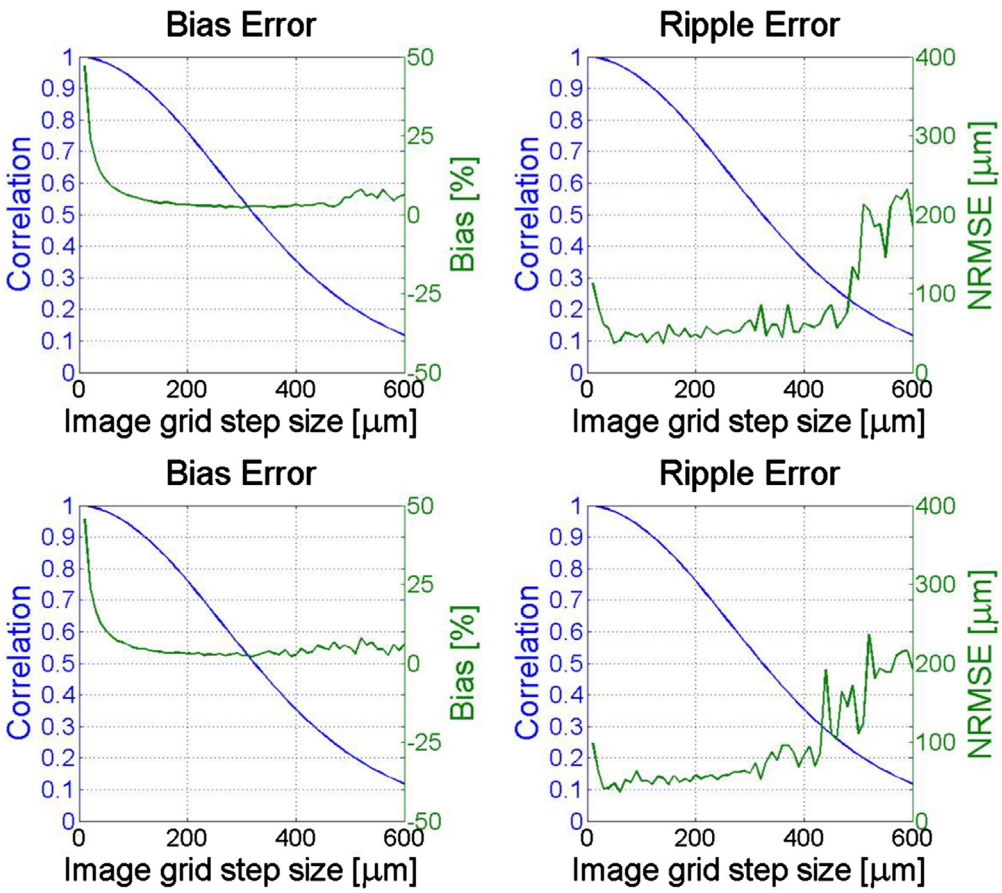

Fig. 8. Position estimation errors (in green) for simulated data of a homogeneous phantom with fully developed speckle (10 scatterers/resolution cell) using fixed *(top)* and adaptive *(bottom)* calibration curves. Cumulative errors (bias) *(left)* and ripple errors *(right)* are presented for different step sizes (distances) of position estimation. The corresponding correlation values of the fixed calibration curve (obtained from the same phantom) are shown in blue. (For interpretation of the references to colour in this figure legend, the reader is referred to the web version of this article.)

Table 1
Ranges of position estimation errors within the 150–350 μm range of image grid step sizes for a simulated FDS phantom using fixed and adaptive calibration curves. A plot of the errors as a function of image grid step size is shown in Fig. 8.

Position estimation errors for the fixed and adaptive calibration curves – simulations		
Type of error	Absolute bias error [%]	Ripple error [μm]
Fixed calibration curve	2.1 – 3.9	43.8 – 85.5
Adaptive calibration curve	2.1 – 3.8	46.0 – 87.0

and is to be expected because at these values, small changes in correlation values cause large changes in the estimated distance. Interestingly, the bias error is higher for too small image grid steps, whereas the ripple error is higher for too large image grid steps. Overall, a fairly wide range of image grid step sizes (150–350 μm) can be used to obtain relatively low errors for both bias and ripple, in the cases of both algorithms. The ranges of absolute errors in this range of image grid step sizes are shown in Table 1. As mentioned in Section 3.3.2, we focused our comparison to this range since our aim was only to show that the proposed real-time method has an acceptable performance in a reasonable application range (of step sizes) as compared to the current literature. As Table 1 shows, the errors are considered acceptable for scan conversion.

Fig. 9 shows corresponding results for experimental data, with Table 2 presenting the extrema of absolute errors in the aforementioned 150–350 μm range of image grid step sizes. These errors are around an order of magnitude higher than those in simulations. Since noise in the image creates noise in the correlation values, this is expected to degrade position accuracy, which could be improved in future work by using a larger comparison window size J (Eq. (4)), which would incorporate more correlation values in the algorithm.

Overall, the scan conversion algorithms performed well in the 150–350 μm step size region both for simulations and experiments, with accuracy progressively degrading outside of this region. As mentioned earlier, this is to be expected since accuracy is improved where the corresponding calibration curve has a high slope. However, it is not clear why – for both algorithms – the ripple error in the experimental data shows a strong peak at lower (50–100 μm) step sizes (Fig. 9). Further work using simulations could potentially uncover responsible mechanisms, including the role of local inhomogeneities. Nevertheless, since the phantom experiment confirms that within the high-slope region of the calibration curve, acceptable errors are obtained, the next validation using clinical data uses a step size from this region.

Summarizing the comparison of scan conversion algorithm performances, position estimation errors were similar for the two methods, with 92.94% overlap of error ranges in average for bias and ripple errors in simulations, and 42.83% overlap of error ranges in experiments (as an average of 62.28% overlap for ripple errors and 23.39% overlap for absolute bias errors). As it can be seen in Tables 1 and 2, the use of a fixed calibration curve was leading to slightly higher absolute bias but lower ripple errors. Nevertheless, the main improvement of the former is in its running time. Use of a fixed calibration curve gave a 350 times improvement in running time compared to using an adaptive calibration curve, with the former generating an image from 1000 A-lines in 345 ± 132 ms (using MATLAB on a computer with Intel Core i5 processor, 8 GB RAM).

4.4. Preliminary in vivo human skin experiment

The 20 recorded lesions had 0.7–5.5 mm thickness and 3.1–14.6 mm length. Fig. 10 shows a representative comparison of a human skin lesion image taken with the reference commercial ultrasound imager, and

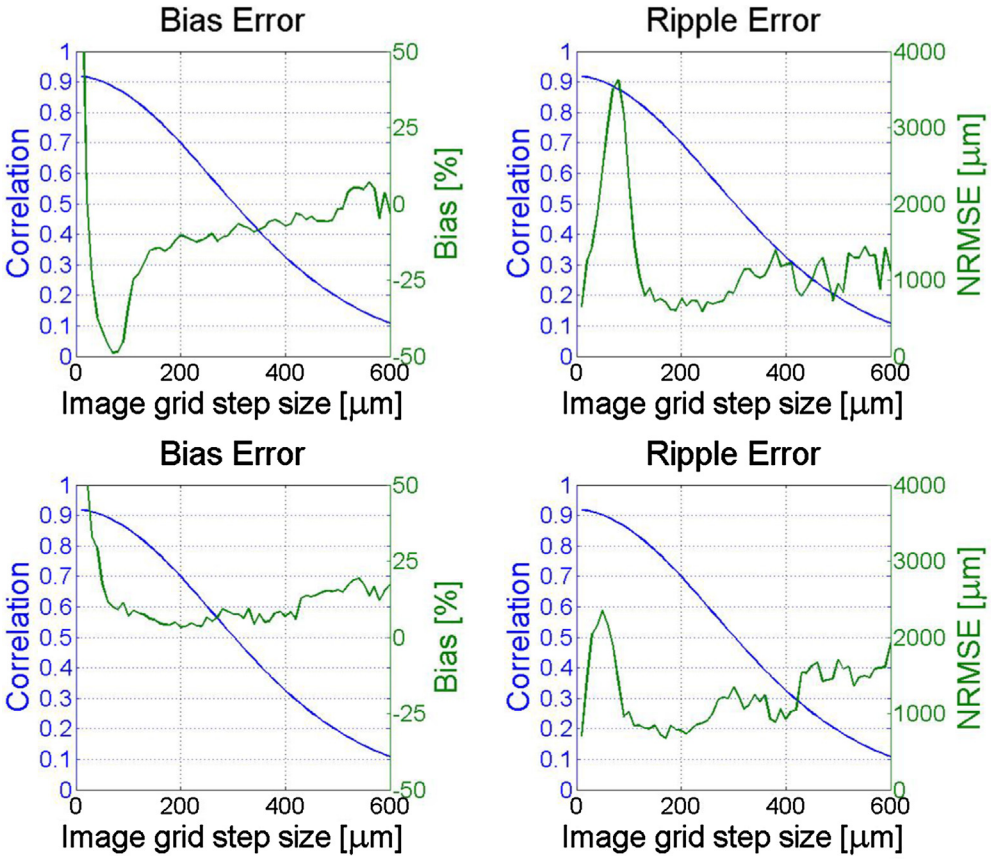

Fig. 9. Position estimation errors (in green) for experimental data of a homogeneous agar-graphite phantom using fixed *(top)* and adaptive *(bottom)* calibration curves. Cumulative errors (bias) *(left)* and ripple errors *(right)* are presented for different step sizes (distances) of position estimation. The corresponding correlation values of the fixed calibration curve (a version of the simulated phantom calibration curve, corrected for noise – see Section 3.2.4) are shown in blue. (For interpretation of the references to colour in this figure legend, the reader is referred to the web version of this article.)

Table 2
Ranges of position estimation errors within the 150–350 µm range of image grid step sizes for the agar-graphite phantom experiment using fixed and adaptive calibration curves. A plot of the errors as a function of image grid step size is shown in Fig. 9.

Position estimation errors for the fixed and adaptive calibration curves – experiments		
Type of error	Absolute bias error [%]	Ripple error [µm]
Fixed calibration curve	6.5–15.7	589.5–1143.0
Adaptive calibration curve	3.3–9.4	674.3–1342.1

Table 3
Scan conversion algorithm performance for *in vivo* (human skin tissue) data based on 20 lesion dimensions with reference dimensions obtained from images obtained using the reference commercial ultrasound device.

Human skin lesion dimension measurements		
Type of error	Mean error [%]	Standard deviation [%]
Lesion length (fixed calibration curve)	10.8	8.6
Lesion length (adaptive calibration curve)	13.2	8.8
Lesion thickness	8.6	6.7

the image obtained with moving a single element transducer by free hand using the proposed scan conversion algorithm. As shown on the right image (which depicts the selection of A-lines from the incoming stream of A-lines) the algorithm could handle a range of scanning speeds. Qualitatively, both sets of images appeared to show the same morphology, as can be seen by a representative set of images in Fig. 10. For a quantitative judgment of the performance, Table 3 shows a summary of length and thickness errors, regarding measured lesion dimensions for all 20 cases, with measurements from the reference device images used as reference. The proposed scan conversion algorithm using a fixed calibration curve performed no worse than the adaptive calibration curve implementation, and its accuracy was close to the thickness measurement errors. The mean error obtained in these

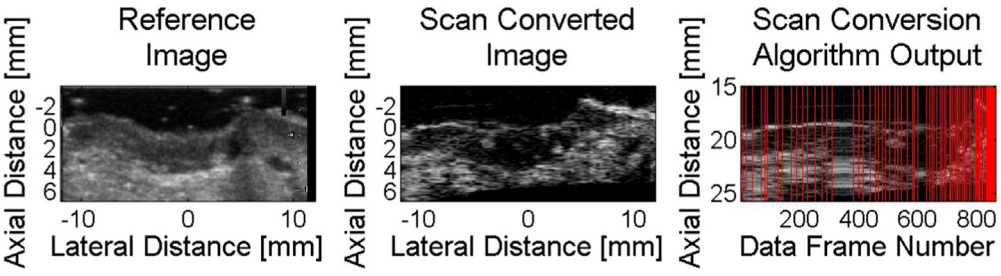

Fig. 10. *In vivo.* ultrasound images of a melanoma on a human sole. *Left:* Ultrasound image obtained with a commercial imaging device using a linear array transducer (Section 3.1.3) as reference. *Middle:* Ultrasound image of the same lesion obtained with a single element transducer using the proposed scan conversion algorithm. *Right:* Set of A-lines (scanned by the single element transducer) after axial shift correction but prior to (lateral) scan conversion. Red lines depict A-lines that were selected for scan conversion (see image in the middle). (For interpretation of the references to colour in this figure legend, the reader is referred to the web version of this article.)

non-homogeneous tissues was similar to the bias error obtained in the phantom image. The results suggest that using the FDS calibration curve on the proposed algorithm generates clinically interpretable images with reasonable position accuracy.

4.5. Remarks on the feasibility of the proposed DABAS method

The results were presented for a specific case, however they can be easily generalized for transducers with different frequencies and pulse parameters. For the specific case presented here, axial image resolution was 135 μm and lateral resolution was 550 μm in the focal region of the transducer. As concluded from Section 4.3, optimal performance of the proposed scan conversion algorithm can be achieved by using an image grid step size being close to this value.

The speed limit of the transducer movement – as seen in Section 2.5 – can be derived from the image grid step size and from the pulse repetition frequency (PRF). For the US-KEY, the effective PRF taking into account data transfer rate was 67 Hz. In the case of the clinical experiments presented in this work, the speed of lateral scanning was 2.27 ± 0.57 mm/s. This means that on average, an oversampling of $n = 8.85$ (Eq. (7)) was achieved.

When talking about the feasibility of a freehand imaging method, another issue to consider beside spatial and temporal resolution (and, in connection, transducer movement speed requirements) is transducer movement requirements in terms of stability of orientation. Instabilities in transducer orientation during freehand scanning can be divided into two groups: axial vibrations and tilting vibrations.

We developed a simple, real-time, correlation-based method to compensate for axial vibrations during freehand frame acquisition (see Section 3.1.3). This compensation was successfully applied on clinical data where axial correction was performed on raw data prior to application of the lateral scan conversion algorithm. The RMSE (root-mean-square-error) of the corrected axial movements was 1.32 mm in average for the 20 recorded lesion cases presented in this article.

Tilting vibrations (or angle distortions) were not investigated in particular, however, we found that – for the clinical experiments presented in Section 4.4 which may have included some tilting motion – results do not suggest its extent to be significant. This is partially due to the design of the imaging hardware which was shaped in a way to minimize tilting vibrations during movement of the transducer.

5. Conclusions

A novel real-time algorithm was presented in this article for data-based scan conversion of A-lines obtained from a laterally scanned ultrasound transducer. The algorithm depends on the calculation of a calibration curve that describes the level of decorrelation between data as the transducer moves away from its original position. Simulations showed that there is negligible difference in the calibration curve for different scatterer concentrations (0.2–10 scatterers/resolution cell). Additive Gaussian noise (−5 to 20 dB SNR) lowered the peak correlation value as expected, however on normalization, the calibration curve retained its original shape. The placement of a relatively few (31) scatterers on a 30 mm axial line around the transducer focus also estimated the curve with high accuracy. Furthermore, good agreement was found between the simulated and experimental calibration curve obtained from simulated and experimental data.

When running the scan conversion algorithm using the calibration curves with a window size of 1, reasonable performance was achieved for simulations, with bias and ripple errors not exceeding 3.9% or 85.5 μm, respectively for a wide range of image step sizes (150–350 μm, where the calibration curve had a high slope). Worse performance was obtained with experimental data (<15.4% absolute bias and <1143.0 μm ripple over the same range of image step sizes), suggesting the need for investigating the use of larger ($J > 1$) comparison window sizes in the algorithm.

Clinical data of *in vivo* human skin lesions showed the feasibility of the proposed scan conversion algorithm for real, non-homogeneous tissue.

Using a fixed calibration curve compared to an adaptive calibration curve estimation gave similar errors for all investigated cases (simulations, phantom experiments and clinical data), while the former method ran about 350 times faster than the latter.

Although simulations and the phantom experiment did not include tilting motion, freehand scanning of tissue may have included some tilting motion; however, results do not suggest its extent to be significant.

Another issue to consider is the acquisition frame-rate necessary for adequate lateral sampling. For dermatological applications, scan times as long as 1 s are routine [20]. Manually scanning a 20 mm wide lesion over such a duration is deemed feasible; using a step size $\Delta y = 300$ μm and $n = 10$ oversampling requires a *PRF* of 667 Hz according to Eq. (7), which is an acceptable value for the ultrasound electronics. In the present case, a *PRF* of 67 Hz was available, which could still be used with a relatively slower scanning speed of around 2 mm/s, providing an oversampling of $n = 8.85$ (see Section 4.5).

Overall, the current work has demonstrated the feasibility of using a real-time scan conversion algorithm for generating 2-D diagnostic images using a laterally scanned single-element ultrasound transducer. The method proposed here can be useful in ultrasound imaging applications in which cost-effectiveness is an important aspect such as high frequency applications where array transducer fabrication is particularly expensive; and where, additionally, linear scanning is preferred to angular scanning. An example of such an application is point-of-care skin imaging. The current results show that the presented methods can be used reliably in such an application.

6. Declaration of interest

G. Csány and M. Gyöngy have a patent application for the imaging algorithm described in the paper and are seeking to develop a medical device that applies this algorithm.

Acknowledgment

The presented results form part of a research program supported by Pázmány Péter Catholic University grants KAP14-17. The work was also supported by the János Bolyai scholarship of the Hungarian Academy of Sciences, grant PD 121105 of the Hungarian National Research, Development and Innovation Office – NKFIH, EFOP-3.6.3-VEKOP-16-2017-00002 and GINOP-2.1.7-15-2016-02201.

The authors thank Máté Kiss for helping develop the axial shift correction method applied in the preprocessing of clinical data and Krisztián Füzesi for designing and producing the casing of the setup used for clinical data acquisition.

References

[1] B. Nelson, A. Sanghvi, Out of hospital point of care ultrasound: current use models and future directions, Eur. J. Trauma Emerg. Surg. 42 (2) (2016) 139–150.
[2] C.L. Moore, J.A. Copel, Point-of-care ultrasonography, N. Engl. J. Med. 364 (8) (2011) 749–757.
[3] N.J. Soni, R. Arntfield, P. Kory, Point of Care Ultrasound E-book, Elsevier Health Sciences, 2014.
[4] J. Chaniot, B. Sciolla, P. Delachartre, T. Dambry, B. Guibert, Vessel segmentation in high-frequency 2d/3d ultrasound images, Ultrasonics Symposium (IUS), 2016 IEEE International, IEEE, 2016, pp. 1–4.
[5] M.R. Sobhani, H. Ozum, G. Yaralioglu, A. Ergun, A. Bozkurt, Portable low cost ultrasound imaging system, 2016 IEEE International Ultrasonics Symposium (IUS), IEEE, 2016, pp. 1–4.
[6] C. Liu, F.T. Djuth, Q. Zhou, K.K. Shung, Micromachining techniques in developing high-frequency piezoelectric composite ultrasonic array transducers, IEEE Trans. Ultrason. Ferroelectr. Frequency Control 60 (12) (2013) 2615–2625.
[7] K.A. Snook, C.-H. Hu, T.R. Shrout, K.K. Shung, High-frequency ultrasound annular-array imaging. part i: Array design and fabrication, IEEE Trans. Ultrason. Ferroelectr. Freq. Control 53 (2) (2006) 300–308.

[8] A.J. Medlin, A.J.P. Niemiec, Scan line display apparatus and method, US Patent App. 12/674007, April 28 2011.
[9] A. Fenster, D.B. Downey, H.N. Cardinal, Three-dimensional ultrasound imaging, Phys. Med. Biol. 46 (5) (2001) R67.
[10] K.E. Thiele, S.H.-H. Chang, Transducer with Spatial Sensor, US Patent 6517491 (February 11 2003).
[11] A. Dunbar, E. Sobrino, System for ultrasound image guided procedure, US patent App. 13/785951 (September 11 2014).
[12] J.W. Sliwa Jr, S.T. Baba, Method and apparatus for two dimensional ultrasonic imaging, US patent 5690113 (November 25 1997).
[13] Z. Banjanin, C.J. Sanders, Patient-probe-operator tracking method and apparatus for ultrasound imaging systems, US patent 9474505 (October 25 2016).
[14] P.E. Eggers, S.P. Huntley, E.A. Eggers, B.A. Robinson, Method, apparatus and system for complete examination of tissue with hand-held imaging devices, US patent App. 13/854800 (August 29 2013).
[15] G. Costa, A.J. Medlin, A.J.P. Niemiec, Improved scan display, wO Patent 2009/ 149 499 (December 17 2009).
[16] S.G. Bartlett, P.J. Hirschausen, Apparatus and method for medical scanning, US patent App. 12/675473 (December 2 2010).
[17] A.J. Medlin, J. Brydon, M. McCarthy, Medical scanning apparatus and method, US patent App. 12/740127 (October 14 2010).
[18] M.-H. Bae, Hand-held ultrasonic probe, eP Patent 0 927 539 (July 7 1999).
[19] M.A. Bahramabadi, Sensorless out-of-plane displacement estimation for freehand 3d ultrasound applications, Master's thesis, Carleton University Ottawa, 2014.
[20] D. Jasaitiene, S. Valiukeviciene, G. Linkeviciute, R. Raisutis, E. Jasiuniene, R. Kazys, Principles of high-frequency ultrasonography for investigation of skin pathology, J. Eur. Acad. Dermatol. Venereol. 25 (4) (2011) 375–382.
[21] M. Gyöngy, G. Csány, Method for generating ultrasound image and computer readable medium, wO Patent 2016/ 207 673 (December 29 2016).
[22] G. Csány, K. Szalai, K. Füzesi, M. Gyöngy, A low-cost portable ultrasound system for skin diagnosis, in: Proceedings of Meetings on Acoustics 6ICU, Vol. 32, ASA, 2017, p. 020002.
[23] A.H. Gee, R.J. Housden, P. Hassenpflug, G.M. Treece, R.W. Prager, Sensorless freehand 3d ultrasound in real tissue: speckle decorrelation without fully developed speckle, Med. Image Anal. 10 (2) (2006) 137–149.
[24] N. Afsham, M. Najafi, P. Abolmaesumi, R. Rohling, A generalized correlation-based model for out-of-plane motion estimation in freehand ultrasound, IEEE Trans. Med. Imag. 33 (1) (2014) 186–199.
[25] N. Afsham, M. Najafi, P. Abolmaesumi, R. Rohling, Out-of-plane motion estimation based on a rician-inverse gaussian model of RF ultrasound signals: speckle tracking without fully developed speckle, in: Medical Imaging 2012: Ultrasonic Imaging, Tomography, and Therapy, Vol. 8320, International Society for Optics and Photonics, 2012, p. 832017.
[26] F. Dong, D. Zhang, Y. Yang, Y. Yang, Q. Qin, Distance estimation in ultrasound images using specific decorrelation curves, Wuhan University Journal of Natural Sciences 18 (6) (2013) 517–522.
[27] C. Laporte, T. Arbel, Measurement selection in untracked freehand 3d ultrasound, International Conference on Medical Image Computing and Computer-Assisted Intervention, Springer, 2010, pp. 127–134.
[28] J. Conrath, C. Laporte, Towards improving the accuracy of sensorless freehand 3d ultrasound by learning, International Workshop on Machine Learning in Medical Imaging, Springer, 2012, pp. 78–85.
[29] M. Li, System and method for 3-d medical imaging using 2-d scan data, US patent 5582173 (December 10 1996).
[30] N.C. Kim, H.J. So, S.H. Kim, J.H. Lee, Three-dimensional ultrasound imaging method and apparatus using lateral distance correlation function, US patent 6988991 (January 24 2006).
[31] L.Y. Mo, W.T. Hatfield, S.C. Miller, Method and apparatus for tracking scan plane motion in free-hand three-dimensional ultrasound scanning using adaptive speckle correlation, US patent 6012458 (January 11 2000).
[32] C. Laporte, Statistical methods for out-of-plane ultrasound transducer motion estimation, McGill University, 2009.
[33] J.M. Thijssen, Ultrasonic speckle formation, analysis and processing applied to tissue characterization, Pattern Recogn. Lett. 24 (4-5) (2003) 659–675.
[34] J.A. Jensen, Field: A program for simulating ultrasound systems, in: 10th Nordicbaltic Conference on Biomedical Imaging, Vol. 4, Supplement 1, Part 1, Citeseer, 1996, pp. 351–353.
[35] J.A. Jensen, N.B. Svendsen, Calculation of pressure fields from arbitrarily shaped, apodized, and excited ultrasound transducers, IEEE Trans. Ultrason. Ferroelectr. Freq. Control 39 (2) (1992) 262–267.
[36] J.P. Kemmerer, M.L. Oelze, M. Gyöngy, Scattering by single physically large and weak scatterers in the beam of a single-element transducer, J. Acoust. Soc. Am. 137 (3) (2015) 1153–1163.
[37] M.F. Insana, R.F. Wagner, D.G. Brown, T.J. Hall, Describing small-scale structure in random media using pulse-echo ultrasound, J. Acoust. Soc. Am. 87 (1) (1990) 179–192.
[38] R.F. Wagner, Statistics of speckle in ultrasound b-scans, IEEE Trans. Sonics Ultrason. 30 (3) (1983) 156–163.
[39] R. Mallart, M. Fink, The van cittert-zernike theorem in pulse echo measurements, J. Acoust. Soc. Am. 90 (5) (1991) 2718–2727.
[40] P. Hassenpflug, R. Prager, G. Treece, A. Gee, Distance measurement for sensorless 3d us, International Conference on Medical Image Computing and Computer-Assisted Intervention, Springer, 2004, pp. 1087–1088.
[41] W. Smith, A. Fenster, Statistical analysis of decorrelation-based transducer tracking for three-dimensional ultrasound, Med. Phys. 30 (7) (2003) 1580–1591.
[42] H. Rivaz, H.J. Kang, P.J. Stolka, R. Zellars, F. Wacker, G. Hager, E. Boctor, Novel reconstruction and feature exploitation techniques for sensorless freehand 3d ultrasound, in: Medical Imaging 2010: Ultrasonic Imaging, Tomography, and Therapy, Vol. 7629, International Society for Optics and Photonics, 2010, p. 76291D.